Computers and Electronics in Agriculture 166 (2019) 104974

Contents lists available at ScienceDirect

Computers and Electronics in Agriculture

journal homepage: www.elsevier.com/locate/compag

Using distributed compressed sensing to derive continuous hyperspectral imaging from a wireless sensor network

Thomas Hänel*, Thomas Jarmer, Nils Aschenbruck

University of Osnabrück, Institute of Computer Science, Wachsbleiche 27, 49090 Osnabrück, Germany

ARTICLE INFO

Keywords:
Hyperspectral imaging
Compressed sensing
Wireless sensor network

ABSTRACT

Hyperspectral imaging is a powerful and versatile tool to gather geo-information. Currently, main contenders for large-scale imaging campaigns are airplanes and satellites equipped with hyperspectral cameras. However, long-term, continuous monitoring of specific areas is hard to accomplish with these techniques: satellites only pass over areas rarely, airplanes require pilots, and all depend on weather conditions and suffer from regulatory overhead. Ground-based monitoring with a Wireless Sensor Network (WSN) is a promising addition which delivers data more continuously because it may be deployed permanently. But hyperspectral sensors are usually considered too expensive and energy-consuming to be used for a WSN. We suggest an alternative approach, using cheaper multispectral sensors and combining them to get hyperspectral-like spectral resolution while preserving the spatial resolution of the WSN. We evaluate our approach, comparing different algorithms for processing the data on datasets gathered in situ and via remote sensing.

1. Introduction

Hyperspectral and multispectral imaging is a versatile tool for gaining information on the environment. It has been used for a multitude of applications. Some of the most prominent ones may be found in an agricultural context (Dale et al., 2013) where it helps assessing quality, biomass, type of crops, and even spread of crop diseases. Beyond agriculture, it may be used in geology for mapping mineral contents and more (van der Meer et al., 2012). In urban areas, hyperspectral imaging has been used for mapping roofs, parking lots (Dell'Acqua et al., 2004), lighting technologies (Dobler et al., 2016), and more.

Naturally, hyperspectral data is more versatile than multispectral data as it contains more information – the channels of a multispectral sensor usually have to be selected carefully to match the requirements of the application. Although remote sensing from satellites is usually preferable due to global coverage, hyperspectral satellites are still rare. Available data, most notably from the Hyperion sensor of the satellite EO-1, has a low temporal resolution and the satellite was taken out of service in March 2017. Future satellites such as EnMap improve coverage but won't come close to offering global coverage at short time intervals.

Even if there were sufficient satellites to record images where- and whenever one is required, these will often be unusable due to clouds. With the low number of satellites in the past and present, this problem is even harder, because in some areas such as Central Europe satellite overpasses and clear skies rarely coincide. A popular alternative to satellites for obtaining data is air-based remote sensing with airplanes or Unmanned Aerial Vehicles (UAVs). However, both come with quite some organizational overhead and can not be performed continuously. In some areas, the usage of UAVs is even forbidden because of safety and security concerns. In order to perform continuous monitoring as well as to monitor areas unobservable with other methods, a ground-based method is desirable that can be used as an alternative or as an addition to the existing methods. Such a continuous monitoring is useful for various scenarios mainly in research such as for the growth period of plants or monitoring fast variations in the course of a day. Apart from being used for continuous monitoring on its own and filling the gaps in time of satellite-based data, ground-based measurements can also be used for the calibration of satellite-based data.

For environmental monitoring, Wireless Sensor Networks (WSNs) consisting of sensor nodes with known positions distributed in an area is an established solution. However, to the best of our knowledge, no one has tried building a hyperspectral WSN so far. We attribute this mainly to the high costs of hyperspectral sensors. There has been at least one successful multispectral WSN deployment indicating that this is a realistic possibility (Gobbett et al., 2013).

In this paper, we address the challenge of developing a WSN that

* Corresponding author.
E-mail addresses: haenel@uos.de (T. Hänel), tjarmer@uos.de (T. Jarmer), aschenbruck@uos.de (N. Aschenbruck).

https://doi.org/10.1016/j.compag.2019.104974
Received 16 May 2019; Received in revised form 15 July 2019; Accepted 24 August 2019

delivers hyperspectral data without being equipped with hyperspectral sensors. We explore the possibility of using a multispectral WSN for this task. If all multispectral sensors are identical, there is no way to gain information about the missing wavelengths unless external data is used. Therefore, we propose to deploy a combination of different multispectral sensors in what we will call a Multi- to Hyperspectral Sensor Network (M2HSN) instead. We consider the diversification of the multispectral sensors a minor technical challenge as the sensors themselves may remain identical, only the filters need to be varied. Such customizable multispectral sensors are already commercially available[1] for less than 200 USD. However, the variety of filters is not yet sufficient for the approach presented in this paper.

Instead of picking filters specific for the application, we propose picking them randomly in order to get more versatility. The big advantage of this approach is that less a priori knowledge is required about the expected spectra. For the estimation of the spectra, we propose a scheme based on Distributed Compressive Sensing (DCS) (Baron et al., 2009).

Our three core contributions in this paper are (1) proposing the idea of combining different multispectral sensors in a WSN to get a hyperspectral measurement, which we call M2HSN, (2) describing how the data collected in an M2HSN can be processed, and (3) demonstrating the success of an M2HSN on two real-world datasets.

The remaining paper is structured as follows: In Section 2 we give an overview of related work and the underlying algorithms we use. In Section 3 we describe our approach and evaluate it in Section 4. In Section 5, we further discuss the evaluation results. Finally, we draw a conclusion in Section 6.

2. Related work

The related work encompasses WSNs in agriculture, alternative approaches for gaining hyperspectral data from multispectral data as well as the underlying Compressive Sensing related technologies we use for recovering the hyperspectral data. The symbols and variables used throughout the paper are summarized in Table 1.

2.1. Wireless Sensor Networks (WSNs) in agriculture

The long-term deployment of Wireless Sensor Networks (WSNs) on agricultural fields is a promising approach for gaining data to be used in precision farming. It has proven to be particularly challenging due to weather, farming activities, animal damage, and more (Bauer and Aschenbruck, 2018; Hartung et al., 2017; Gobbett et al., 2013). Sensors can be used to sense soil parameters, weather data (Hartung et al., 2017), or attempt to measure plant properties more directly (Qu et al., 2014; Gobbett et al., 2013). We consider the latter particularly insightful because the condition of crops is the most important information for the farmer, while the other sensors provide useful supplementary data. For measuring plant properties, visual light and near infrared have gained increasing attraction (Qu et al., 2014; Gobbett et al., 2013). Among these, sensors that are elevated seem more practical as they are less prone to dirt and animal damage albeit they are more likely to collide with farming equipment. A major challenge for these sensors is the influence of the sun's altitude angle, which has been researched in previous works (Qu et al., 2014; Gobbett et al., 2013) and turned out to be handleable by combining multiple measurements during a day and incorporating the angle.

Previous works concentrated on selected plant parameters. Hyperspectral data, as required by remote sensing, is far more flexible. Therefore, we explore the possibility of acquiring such data in a WSN as well.

[1] https://pixelteq.com/pixel-sensor/.

Table 1
Symbols used in this paper.

Symbol	Description
j	index used for position of nodes in a WSN
x_j	high-resolution spectrum at position j
$\boldsymbol{x}$	concatenation of all x_j
x_s	soil base spectrum
x_w	water base spectrum
x_v	vegetation base spectrum
x_c	average or common spectrum
$x_{\Delta,j}$	the difference between x_j and x_c
$c_{s,j}$	soil fraction at position j
$c_{w,j}$	water fraction at position j
$c_{v,j}$	vegetation fraction at position j
$\boldsymbol{X}$	matrix of high-resolution base spectra
$\boldsymbol{Y}$	matrix of low-resolution base spectra
Y_j	Y for the multispectral sensor at position j
c_j	fraction vector at position j
M	number of channels at low resolution
N	number of channels at high resolution
J	number of nodes
$\boldsymbol{f}$	sparse representation of $\boldsymbol{x}$
f_j	sparse representation of x_j
f_c	sparse representation of x_c
Ψ	transformation matrix for all spectra
Ψ_j	transformation matrix for the j-th node
Ψ_c	transformation matrix for the common part
y_j	low-resolution spectrum at position j
$\boldsymbol{y}$	concatenation of all y_j
Φ	measurement matrix for all spectra
Φ_j	measurement matrix for a single node
Φ_D	difference matrix
Θ	matrix of high-resolution filter spectra
S	number of seeds used in evaluation

2.2. From multispectral to hyperspectral

Due to the high costs of hyperspectral sensors, we instead suggest using sensors with lower spectral resolution. Creating hyperspectral images from images of lower spectral resolution is uncommon as it means adding made-up data. However, it is possible to perform an image fusion of a panchromatic image with high spatial resolution and a hyper- or multispectral image with low spatial resolution, which is called pan-sharpening. In the past, researchers mainly focused on multispectral images (Ehlers et al., 2010; Vivone et al., 2015). However, pan-sharpening of hyperspectral images gained more attraction in the last decades spawned by the launch of hyperspectral satellites such as EO-1. Pan-sharpening can also be used for fusing multi- and hyperspectral data when a panchromatic image is first created from the multispectral data.

Two methods that take a slightly different approach are Universal Pattern Decomposition Method (UPDM) (Liu et al., 2009) and Spectral Resolution Enhancement Method (SREM) (Sun et al., 2015) which fuse multi- and hyperspectral data directly without first creating a panchromatic image. Thus, they increase the spectral resolution of multispectral images by incorporating hyperspectral data from a subset of pixels where it is available. SREM still requires a hyperspectral image but generates a hyperspectral image of higher spatial resolution in a larger area than the one of the original hyperspectral image. UPDM was instead used to simulate hyperspectral images based on multispectral images. It only requires few high-resolution spectra to be known a priori and may, therefore, be adapted for the envisioned M2HSN.

2.3. Universal Pattern Decomposition Method (UPDM)

UPDM represents each spectrum as a linear combination of some base spectra such as soil, water, and vegetation:

$$x_j = c_{s,j}x_s + c_{w,j}x_w + c_{v,j}x_v \tag{1}$$

with the spectrum x_j at position j, the coefficients $c_{s,j}$ of soil, $c_{w,j}$ of water, and $c_{v,j}$ of vegetation which state the fractions of these components and the corresponding base spectra x_s, x_w, and x_v. This may also be expressed in matrix form:

$$x_j = Xc_j \text{ with } X = (x_s \;\; x_w \;\; x_v) \text{ and } c_j = \begin{pmatrix} c_{s,j} \\ c_{w,j} \\ c_{v,j} \end{pmatrix} \tag{2}$$

with the matrix of base spectra X and the fraction vector c_j. At a lower spectral resolution, the coefficients remain the same but the spectra change. Eq. (2) then changes to:

$$y_j = Yc_j \tag{3}$$

with the low-resolution spectrum y_j and the matrix of low-resolution base spectra Y.

The matrix of base spectra need to be known in its multispectral version Y and in its hyperspectral version X. Then, the vector of coefficients c_j is gained from the low-resolution spectra using the pseudoinverse Y^{-1} of Y:

$$c_j = Y^{-1}y_j \tag{4}$$

Lastly, the coefficients are used to gain the hyperspectral representation x_j at the given location by inserting c_j from Eq. (4) into Eq. (2):

$$x_j = XY^{-1}y_j \tag{5}$$

As only the base spectra, albeit in two representations, are required, the a priori knowledge put into the process is reduced in comparison to pan-sharpening approaches which require hyperspectral images.

2.4. Compressive sensing

Compressive Sensing has first been presented in Donoho (2006) and opened up the way to a new, more efficient concept of data acquisition by compressing the data during acquisition instead of afterwards. The following description has been mostly based on (Candes and Wakin, 2008): The general idea of Compressive Sensing is measuring a smaller data vector y of length M and reconstructing an original vector x of length N with $N \gg M$ from it by incorporating the information that x is sparse in some given domain.

This translates into equations as follows: f is some sparse vector with few non-zero values that is related to x with a linear transform:

$$x = \Psi f \tag{6}$$

with the transformation matrix Ψ. The compressed vector y is acquired directly using some measurement process that may be expressed as a matrix multiplication:

$$y = \Phi x \tag{7}$$

where Φ is called the measurement matrix. Inserting Eq. (6) in Eq. (7) gives us the equation that needs to be approximately full-filled by the estimate $f_{estimate}$ for f. Combining this with the second requirement of $f_{estimate}$ being sparse leaves us with the problem to solve:

$$f_{estimate} = \underset{f'}{\operatorname{argmin}} ||f'||_0 \text{ with } y \approx \Phi\Psi f' \tag{8}$$

where $||\cdot||_0$ denotes the ℓ_0-norm, i.e. the number of non-zero elements, and the '≈' sign denotes that the equation usually won't be perfectly full-filled due to noise. Various solvers have been developed for problems of this kind. Many are based on replacing the ℓ_0-norm with the ℓ_1-norm, which gives the same result with overwhelming probability. This leads to a convex problem that may be solved using linear programming (Candes and Wakin, 2008). A Bayesian solver named BCS was developed in (Ji et al., 2008). The solver SL0 was developed in (Mohimani et al., 2009). It is based on iteratively transitioning from the ℓ_2-solution obtained using the pseudoinverse to an ℓ_0-solution by changing the norm itself.

Common transform matrices are those of the Discrete Cosine Transform (DCT), Discrete Fourier Transform (DFT), or various variants of the Discrete Wavelet Transform (DWT). For piece-wise constant vectors, a matrix that describes f as the element-wise difference of x or inversely x as the cumulative sum of f similar to the *Horz-diff* matrix (Quer et al., 2009) may be sufficient:

$$\Psi_D = \begin{pmatrix} 1 & 1 & \dots & 1 & 1 \\ 0 & 1 & \dots & 1 & 1 \\ \vdots & \vdots & \ddots & \vdots & \vdots \\ 0 & 0 & \dots & 1 & 1 \\ 0 & 0 & \dots & 0 & 1 \end{pmatrix} \tag{9}$$

Note, that this may also be expanded to the difference of the difference similar to the second derivative for functions $\Psi_{D2} = \Psi_D\Psi_D$ or even to any higher degree $\Psi_{DN} = \Psi_D^N$.

The main challenge in using Compressive Sensing is designing a suitable measurement process. This process has to acquire y according to Eq. (7) without acquiring x before. Note, that if x was acquired before and Eq. (7) simply calculated, one would merely perform a normal compression. Designing Φ is relatively easy as random matrices such as a Gaussian matrix with all elements drawn from a Gaussian distribution have been shown to be compatible with most transformations with high probability. Very convenient solutions are possible when choosing a sparse Φ, i.e. just picking values randomly out of x. This has been shown to be sufficient in many cases (Rudelson and Vershynin, 2006).

2.5. Distributed Compressive Sensing (DCS)

In order to expand Compressive Sensing to multiple dimensions such as in a spatial distribution typical of WSNs, two solutions stand out: Kronecker Compressive Sensing (KCS)(Duarte and Baraniuk, 2012) and DCS (Baron et al., 2009).

KCS requires a transform for each dimension and has shown some success for scalar fields (Hänel and Aschenbruck, 2017). For hyperspectral data, DCS seems more suitable as it assumes similar vectors at multiple locations without introducing further transforms for the spatial dimensions. DCS encompasses three different models for the similarity between the vectors called Joint Sparsity Models (JSMs). JSM-1 assumes a sparse common component and a sparse additive innovation per location, JSM-2 assumes a shared support, and JSM-3 assumes a non-sparse common component and a sparse additive innovation. Thereof JSM-1 seems most suitable for spectra as they are piece-wise constant and the same holds true for the differences. Furthermore, JSM-2 and JSM-3 require customized solvers, whereas JSM-1 is compatible with any solver suitable for Compressive Sensing. For those reasons, we limit our considerations to JSM-1 from here on. In JSM-1, the data for each position is modeled as

$$\begin{aligned} x_j &= x_{\Delta,j} + x_c \\ x_j &= \Psi_j f_j + \Psi_c f_c \end{aligned} \tag{10}$$

where $x_{\Delta,j}$ denotes the innovation at position j, x_c the common part, Ψ_j the transform matrix for position j, and Ψ_c the transform matrix for the common part. The second row was obtained by inserting Eq. (6).

For a total of J sensors, vectors combining all positions may be defined:

$$\begin{aligned} x &= (x_1^T, x_2^T, \dots, x_{J-1}^T, x_J^T)^T \\ y &= (y_1^T, y_2^T, \dots, x_{J-1}^T, y_J^T)^T \\ f &= (f_c^T, f_1^T, f_2^T, \dots, f_{J-1}^T, f_J^T)^T \end{aligned} \tag{11}$$

with x being of length $J{\cdot}N$, y of length $J{\cdot}M$, and f of length $(J+1){\cdot}N$. This allows formulating a joined Ψ of size $(J{\cdot}N) \times ((J+1){\cdot}N)$:

$$\Psi = \begin{pmatrix} \Psi_c & \Psi_1 & 0 & \dots & 0 \\ \Psi_c & 0 & \Psi_2 & \dots & 0 \\ \vdots & \vdots & \vdots & \ddots & \vdots \\ \Psi_c & 0 & 0 & \dots & \Psi_J \end{pmatrix} \tag{12}$$

With these vectors a combined Φ with a size of $(M{\cdot}J) \times (J{\cdot}N)$ may be defined:

$$\Phi = \begin{pmatrix} \Phi_1 & 0 & \dots & 0 \\ 0 & \Phi_2 & \dots & 0 \\ \vdots & \vdots & \ddots & \vdots \\ 0 & 0 & \dots & \Phi_J \end{pmatrix} \tag{13}$$

with Φ_j being the measurement matrix of the j-th position.

3. Multi- to Hyperspectral Sensor Network (M2HSN)

An M2HSN consists of sensor nodes with multispectral sensors. The sensor nodes are connected in a WSN. The multispectral data of the whole WSN is collected to then estimate hyperspectral data from it. This estimation process can be based on DCS or UPDM. Before discussing the estimation process we first describe the sensor nodes and the network.

3.1. Sensor nodes

First, sensor nodes have to be prepared, e.g., as shown in Fig. 1 on the right. Each node has a multispectral sensor. Albeit not being the only possible architecture, in this paper we assume the multispectral sensor to consist of M light sensors (e.g., photodiodes). The light sensors are connected to an Analog-to-Digital Converter (ADC) which supplies a Central Processing Unit (CPU) with digital readings of each sensor, that are then transmitted to a fusion center. Each light sensor needs to be covered with a filter. The choice of the filters depends on the requirement for the hyperspectral resolution. From this requirement, one may deduce the number of channels N to be included in the output data generated by the fusion center. This equals the number of bands which would be acquired by aerial or satellite-based remote sensing. Filters of all N channels need to be available for this approach to work. For each sensor node, each of the M light sensors is covered with a filter picked at random from the N different filter types.

In order to measure the reflectance, it makes sense to put the sensor in a slightly elevated position, such as on a post, pointing downwards. The angle of view of the light sensors should be sufficiently wide to ensure averaging over a sufficiently wide area. Neither should the angle be too wide as light from the sides may disturb the measurement. If the angle of view of the sensors is too narrow or to wide, a diffuser or an aperture may be added.

3.2. Sensor network

An example network of $J = 4$ sensor nodes is shown in the left part of Fig. 1. In a real network, the number of sensor nodes J depends on the size of the area that shall be monitored, the required spatial resolution, and the required estimation quality of the hyperspectral data.

Each sensor node is prepared as described in the previous subsection. Note the different filter combinations shown in Fig. 1. The sensor nodes can be placed in the given area using different patterns: They may be placed at areas of interest, on a grid, or randomly. The grid pattern allows for generating images similar to those of a satellite.

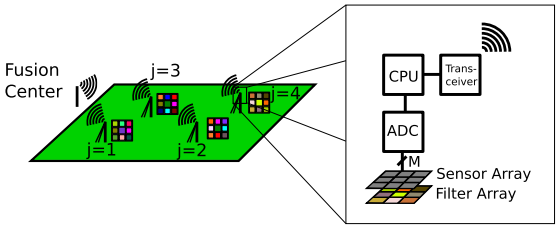

Fig. 1. Sensor node and network architecture of an M2HSN.

Each sensor node sends its readings of each light sensor to a fusion center at a frequency depending on the required temporal resolution. With the amount of data being lower in comparison to hyperspectral data, the transmission time is also lower, leading to reduced power consumption and, thereby, a prolonged lifetime of the sensor node. The frequency of measurements will usually be on a scale of hours, making synchronization challenges, bandwidth requirements, and the calculation time for the estimation of the high-resolution spectrum negligible. This allows us to describe the data acquisition as taking a snapshot of the whole area. Each snapshot may be recorded independently from snapshots at other times. The data collection for one snapshot can be done using any communication pattern: it may happen in a multi- or single-hop pattern or even via the internet.

3.3. Hyperspectral data estimation

The main task in processing is the estimation of the hyperspectral data. If the resources of the fusion center are insufficient, this estimation may also be outsourced to a high performance computing cluster. As the general idea of an M2HSN is new to the best of our knowledge, there are no existing algorithms to compare against. It seems unreasonable to develop a completely new algorithm instead of relying on previous research results in signal processing and remote sensing. Therefore we modify existing algorithms to be used for an M2HSN, yielding three different approaches for the estimation: (1) interpolation, (2) UPDM, and (3) DCS. The interpolation is independent for each location and consists of a simple linear interpolation between the channel readings.

UPDM is applied by measuring the base spectra in advance and then independently applying the algorithm to the multispectral data. It may be used for random channels as well, when the matrix of base spectra Y is known for each combination of filters. As each combination should ideally be unique, this will usually result in one matrix per node, i.e. replacing Y in Eqs. (3) and (4) with Y_j.

The data processing based on DCS uses JSM-1. Ψ is generated using Eq. (12) with $\Psi_c = \Psi_1 = \Psi_2 = \dots = \Psi_J = \Psi_D$ with Ψ_D being the difference matrix from Eq. (9). The Φ_j constructing Φ according to Eq. (13) are directly deduced from the filters used in sensor node j according to $\Phi_j = \Phi'_j\Theta$. Each Φ'_j consists of the M rows of an $N \times N$ identity matrix corresponding to the M out of N filters used on the sensor node. The $N \times N$ sized Θ contains the transmission spectra of the filters. From here on we assume ideal narrow-band filters by setting Θ to the identity matrix and $\Phi_j = \Phi'_j$ respectively. y contains the concatenated channel readings from all sensors. The combined Φ, Ψ, and y are used in Eq. (8):

$$f_{estimate} = \underset{f'}{\operatorname{argmin}} \|f'\|_0 \text{ with } y \approx \Phi\Psi f' \tag{14}$$

Out of the above mentioned solvers, we use SL0 (Mohimani et al., 2009) which offers a good trade-off between reconstruction quality and speed in our experience. A comparison of solvers is beyond the scope of this paper. Furthermore, the choice of the solver has a relatively small influence on the result in our experience.

The result $f_{estimate}$ may be inserted into Eq. (6) to get the concatenation of all high-resolution spectra $x_{estimate}$:

$$x_{estimate} = \Psi f_{estimate} \tag{15}$$

4. Evaluations

Currently, the availability of narrowband filters at a broad range of wavelengths and the availability of photodiodes with a sufficient spectral range are limited in ready-to-use solutions. This makes the realization of the approach difficult. Suitable ready-to-use solutions

Table 2
Parameters of the datasets used in the evaluation.

Source	Area [km^2]	Pixel size [m^2]	# Spectra	N	Spectral range [nm]
Ground	3.5 × 3.5	<1	124	48	400.4–1099.2
Airplane	6 × 2.7	9	1.8×10^6	49	406.1–1107.5
Satellite	10 × 100	900	9.4×10^5	92	396.3–1104.2

may become available in the near future. An alternative would be building such a system from scratch. Prior to spending this effort, it is desirable to get an estimate on the potential of such a system by means of trace-based simulations which we supply in this paper. Three datasets as listed in Table 2 will be used, the first one has been measured directly on the ground in wheat fields with a spectrometer and will give an insight of how spectra typically look when acquired directly in situ. The second dataset has been acquired using a hyperspectral camera on an airplane and can be used for evaluations at a larger scale. The third dataset has been acquired by satellite. The main advantage of this third dataset is its availability which facilitates reproduction of the results.

4.1. In situ data

We first evaluate the approach on reflection spectra from wheat which have been acquired on the ground with a spectroradiometer (HR-1024i by Spectra Vista Corporation). We consider a total of 124 wheat spectra acquired at different times and locations from an area of approximately 3.5 km × 3.5 km, giving a good overview on how wheat spectra vary. The spectrometer acquires data between 350 nm and 2500 nm. Thereof, we consider the 482 channels with center wavelengths from 400.4 nm to 1099.2 nm to match the range typical of silicon-based photodiodes (400 nm to 1100 nm) as close as possible. These are light sensors suitable for low-cost sensors. For an increased wavelength range, significantly more expensive sensors are required. We investigate one sample reflectance spectrum. It is shown as a black curve in Fig. 2. The blue, green, and red vertical lines show the wavelengths of the corresponding colors in visible light and are included for orientation. The spectrum is dominated by a step near the color red and the border of visible and infrared light. It is called red edge and serves as an important indicator for the condition of plants (Mulla, 2013). In visible light below 700 nm the reflectance is lower and in infrared light above 700 nm the reflectance is higher. In both ranges, the variations are smaller but still contain features important for gaining information on the plants. No significant variations occur for very small wavelength changes. This implies that the 482 channels in the relevant spectral range are significantly more than necessary.

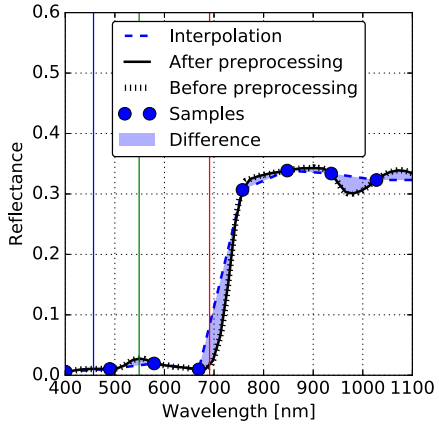

Fig. 2. Preprocessing of a high-resolution spectrum and qualitative evaluation of its reconstruction from a low-resolution spectrum using interpolation.

As we want to concentrate on how far we can reduce the resolution, we first reduce it by throwing away redundant values so we can concentrate on the harder part of resolution reduction. In this preprocessing step we keep $N = 48$ channels. The channels are selected such that the center wavelengths are closest to equidistant wavelengths. This was not given in the original data as it is common to make channels wider at high wavelengths because energy density is lower in this range in the spectrum of the sun. This is not necessary in a stationary M2HSN as the light sensors can instead be configured individually to collect photons for a longer time at long wavelengths. Both the spectra before and after preprocessing are shown in Fig. 2 as a black dotted curve and as a black solid curve. They barely differ, showing that the resolution reduction kept all the relevant information. The resolution after preprocessing is what we call the hyperspectral resolution from here on.

For the multispectral version, we begin the evaluation with $M = 8$ approximately equidistant channels. Eight channels are a convenient choice because many ADCs offer eight channels. Using linear interpolation, the samples and the result are shown for the example spectrum in Fig. 2 in blue. The differences to the spectrum at the hyperspectral resolution are highlighted in a lighter blue. Some extrema got cut off, making the resulting spectra unsuitable for many tasks.

For a qualitative comparison, we perform DCS on all $J = 124$ spectra which gives the results shown in Fig. 3. For the following evaluations we use the Root Mean Square Error (RMSE) between the original spectrum and the calculated spectrum. It is defined as follows:

$$RMSE = \sqrt{\frac{(x_{estimate,j} - x_j)^2}{N}} \tag{16}$$

Such a metric is better suited than a comparison of resulting soil or plant metrics as it evaluates the spectrum in all channels and making all channels available is the main purpose of the approach. The channels sensed by the sensors are now selected randomly and again shown with blue markers. The best spectrum, the median spectrum, and the worst spectrum as indicated by the RMSE are shown as solid blue curves to give an overview of the effects. The original spectrum (dashed blue), the mean spectrum or common part (dashed black), and its estimate (solid black), which is a by-product of JSM-1, calculated as $x_c = \Psi_D f_c$, are included for comparison. The best result as well as the common part include all relevant features of the spectrum, deviations are negligible. The mediocre spectrum is just as good across most wavelengths, only the range near the red edge shows some deviations at approximately 750 nm. In the worst spectrum, the reflectance in the range between 700 nm and 900 nm has been significantly underestimated. We attribute this to the lack of samples in this range and thereby defaulting to values closer to the common part. Additionally, there are some smaller differences. This indicates that the data may at some sensor nodes get insufficiently reconstructed in parts of the spectrum. However, these deviations may be identified during evaluation of experts or in an automated process by finding discrepancies over time, space, or wavelength.

If the spectrum behaves un-normally for a short time this may indicate a problem with the estimate. If it differs drastically from its spatially neighboring sensor nodes, this may be an indicator as well. Many plant properties can be extracted from features at multiple wavelengths. If the features at different wavelengths indicate contradicting information on a plant property, this is an indicator for a bad estimation as well.

For a more thorough comparison of linear interpolation and DCS, we have repeated the calculation for different values of M as well as 100 different seeds for the spectrum selection. The results for both DCS and interpolation are shown in Fig. 4. Each box of the boxplot contains the RMSEs of all combinations of spectra and seeds, a total of 12,400 values per box. The RMSE decreases with increasing M for both variants. The RMSE of DCS is significantly lower than for the interpolation, demonstrating the benefit of incorporating multiple spectra to get a better

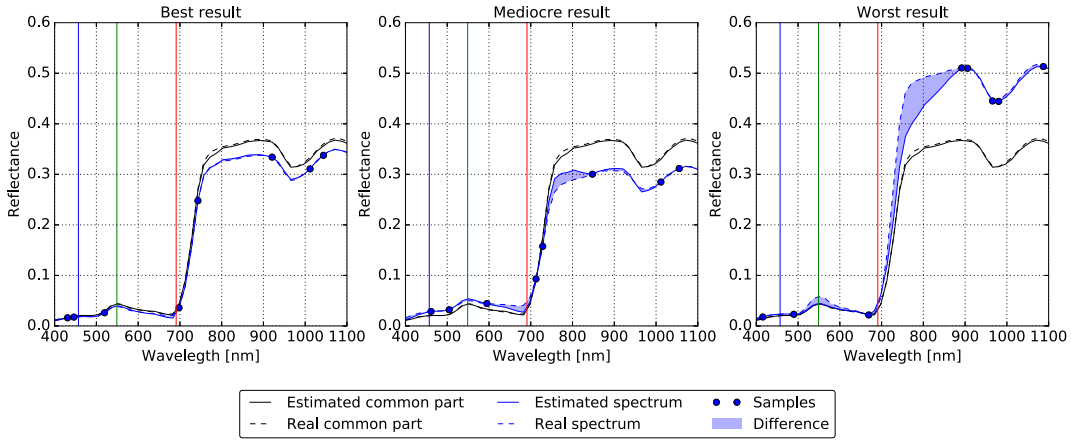

Fig. 3. Qualitative comparison of the hyperspectral estimate using DCS in comparison with the original data for the minimal, median, and maximal RMSE.

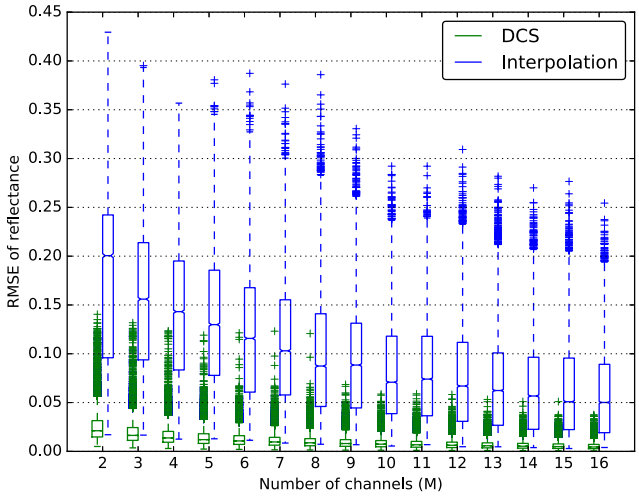

Fig. 4. Quantitative comparison of DCS and linear interpolation at different multispectral resolutions for ground-based measurements.

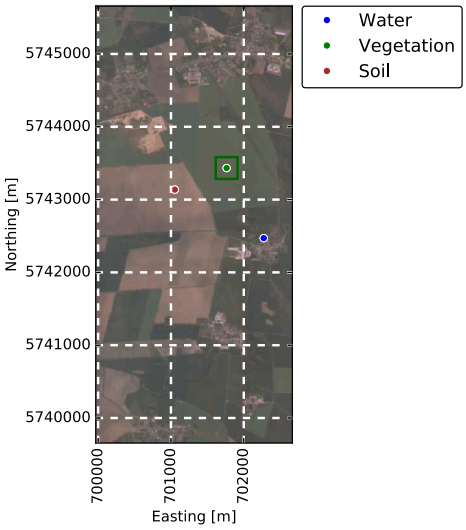

Fig. 5. Image from hyperspectral remote sensing data used for larger scale evaluation. The locations for UPDM base spectra are indicated by points. The green square indicates the area used for vegetation-only evaluation. (For interpretation of the references to colour in this figure legend, the reader is referred to the web version of this article.)

estimate. As it was mainly designed for remote sensing data, we defer the evaluation of UPDM to the next datasets.

4.2. Aircraft-based remote sensing data

The second dataset has been acquired by airplane in a rural area in the east of Germany with a hyperspectral camera (HySpex VNIR-1800 by Norsk Elektro Optikk). Fig. 5 shows an image generated from the hyperspectral data. The area of 6 km × 2.7 km contains agricultural fields with and without plants, forests, and small villages, giving a representative mix found in rural areas. There is also a small lake covered by the blue marker, making all base spectra available which are necessary for UPDM. The coordinates refer to Universal Transverse Mercator (UTM) zone 32 N. The image has a spatial resolution of 3 meters per pixel and a total of 122 spectral channels between 406.1 nm and 2482.2 nm. As for the in situ data, we only use the $N = 49$ channels up to 1107.5 nm to match the range of silicon-based photodiodes. Both the spectral range and the spectral resolution approximately match those of the in situ data. We fix M to 8 and vary the number of sensor nodes J. For each value of J, we pick J pixels randomly from the map, serving as sensor node locations, and repeat this selection of pixels with $S = 100$ different seeds.

We calculated the estimates for the high-resolution spectrum using all three algorithms. For interpolation and DCS the procedure is the same as in Section 4.1. For UPDM, we extracted the base spectra of soil, vegetation, and water directly from the map at the locations indicated in Fig. 5.

The resulting RMSEs are shown in Fig. 6a. Each box of the boxplot contains the RMSE for all positions at all seeds, a total of $J \cdot S$ values per box. For UPDM, the RMSE is highest and varies the most. This may be attributed to the problem that the spectra at some locations are not well-representable with the base spectra. The interpolation and DCS results are significantly better. The DCS results are the best for approximately $J \geqslant 20$. This shows clearly that DCS profits from incorporating measurements from multiple locations. In contrast to DCS, the RMSE for interpolation and UPDM is independent from J. For approximately $J \geqslant 40$ the DCS results show few further improvements.

As WSNs will often be deployed in more homogeneous areas, such as an agricultural field with only one type of crops, we limited the evaluation to such an area in the next step. The area of 300 m× 300 m is indicated by a green square in Fig. 5 and the result is shown in 6b.

The interpolation performs much worse because vegetation spectra show more variations and are thereby more difficult to approximate with an interpolation than other spectra such as soil or water. UPDM

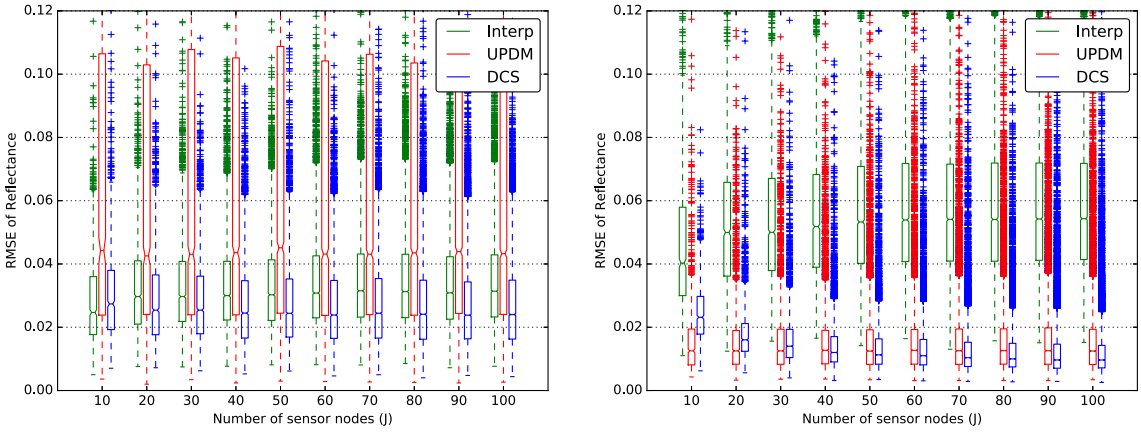

(a) Data selected from the whole map.

(b) Data selected from the square containing solely vegetation.

Fig. 6. Comparative evaluation of the high-resolution spectrum reconstruction using interpolation, UPDM, and DCS on aircraft-based remote sensing data.

performs much better as the spectra are better describable by the base spectra and it delivers the best result for a small number of sensor nodes. It is outperformed by DCS for approximately $J \geqslant 40$. DCS's overall quality is better than for the whole area (see Fig. 6a) as the spectra are more similar, making the common part of JSM-1 a more appropriate assumption.

4.3. Satellite-based remote sensing data

The third dataset has been acquired by the EO-1 satellite with the hyperspectral camera Hyperion. Although having quality issues in comparison to the previous datasets due to an incomplete calibration of the channels and some channels not being operative, we included this dataset for assessing the approaches when dealing with faulty data and at an even larger scale. Furthermore, the data is freely available[2], allowing for a reproduction of the results.

The area has a size of approximately 10 km × 100 km and contains a mixture of urban areas, forests, wetlands and mostly agricultural areas. An image generated from the hyperspectral data is given in Fig. 7a. It has a spatial resolution of 30 m and a total of 242 channels in the range from 355.6 nm to 2577 nm. We processed the data as for the previous datasets and select the $N = 92$ channels between 396.3 nm and 1104.2 nm for the evaluation. For atmospheric correction, dark object subtraction assuming the dark object marked in the map has been applied. The evaluation follows the same pattern for the airborne data with a fixed number of $M = 8$ channels per sensor node and a varying number of sensor positions J picked at random with $S = 100$ different seeds per value of J. The resulting boxplots are shown in Fig. 7b. It shows the RMSE of the radiance instead of the reflectance due to the incomplete calibration. For interpolation and DCS, all outliers are included in the figure. For UPDM, several outliers are significantly higher. The median of the RMSE for the interpolation is the highest. UPDM yields medium RMSEs while DCS achieves the lowest RMSE and again benefits from an increased number of sensors. UPDM's mediocre performance in comparison to the good performance in the vegetation-only evaluation on the airborne data and the bad performance on the mixed evaluation on the airborne data may be explained by the relatively high percentage of area covered by vegetation as shown in Fig. 7a.

Besides the median RMSE, the spread of the RMSE is important, too. It indicates how reliable a low RMSE can be achieved. For UPDM, the spread is very high and the above mentioned outliers clearly indicate, that the error is significantly higher than with interpolation, albeit only in a few pixels. This may be attributed to some pixels not being describable as a composition of the base spectra. Overall, DCS generates the lowest errors at high reliability while UPDM is highly dependent on the choice of base spectra matching the whole area to be evaluated.

5. Discussion

The evaluation results allow for a more thorough discussion of design choices when realizing an M2HSN. First, we can make a more informed statement on the scale of the network. In both remote sensing datasets using more than approximately 40 sensors nodes did not generate further RMSE improvements which opens up a way to improve the scalability of the calculation: The sensor network may be partitioned in groups of approximately 40 sensor nodes and DCS may then be applied to each group of nodes separately at low loss of estimation quality. With respect to the calculation time, which is higher for DCS, such a partitioning helps reducing the overall calculation time for large networks.

Note that the improvement up to 40 sensor nodes shall not be used to draw a conclusion such as: more sensor nodes have to be deployed to obtain an improved spectral reconstruction. Instead, the number of sensor nodes will be dictated by the required spatial resolution. If more than 40 nodes are necessary for the desired spatial resolution, the spectrum reconstruction will be good as well with DCS. For a smaller number of nodes, UPDM is a better choice, if the base spectra are well-chosen. If that is not possible, more spectral channels or even an actual hyperspectral sensor on each sensor node may be necessary.

Besides the number of nodes, the viewing angle of the sensor and thereby the surface area sensed by this sensor needs to be chosen as discussed in Section 3.1. The evaluations showed that the approach works for a great range of sensed surface areas with 900 m^2 in the satellite data, 9 m^2 in the airborne data, and less than 1 m^2 in the in situ data, introducing no stricter limits on the choice of the viewing angle.

The number of spectral channels enables an estimate for the communication requirements. Eight channels turned out to be a good compromise. Assuming 16 bit ADCs, this totals at 16 Bytes per reading. Timestamps are not necessary - due to the soft timing requirements, the reception timestamp at the fusion center will suffice. Information about location and selection of channels are also not required because they can be stored at the fusion center.

Nevertheless, out of the stored information, the fusion center has to select the part corresponding to the transmitting node. Therefore, an identifier needs to be added to the transmitted data, raising the total payload of a message to 17 or 18 bytes. However, such an identifier is already included in many protocols (e.g. MAC-address, IP-address, host name).

After all, the tiny amount of data allows for the use of communication technologies that provide high energy efficiency at the cost of

[2] https://earthexplorer.usgs.gov/, Entity ID: EO1H1960232013159110KF_SG1_01.

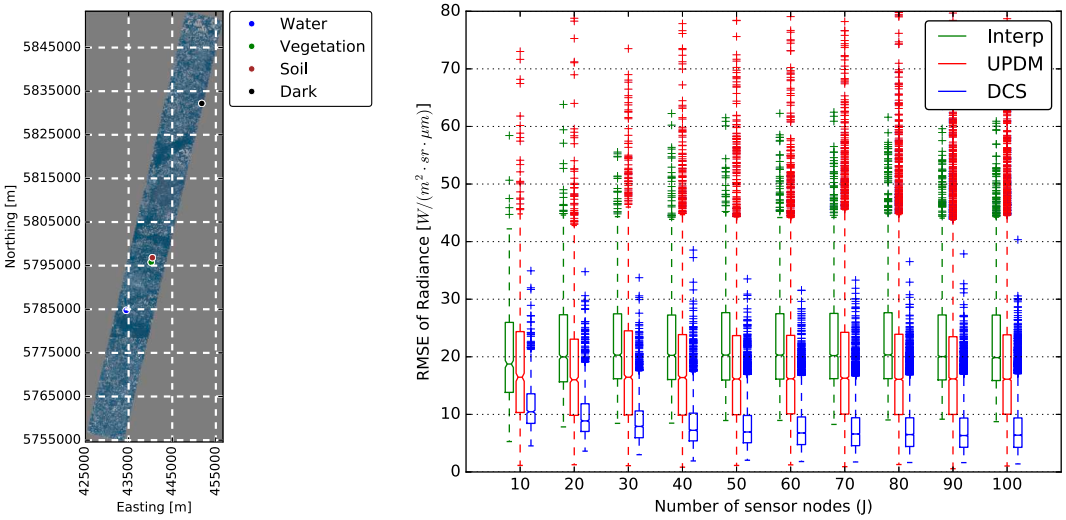

(a) Map with locations of base spectra and dark object marked.

(b) Evaluation results using interpolation, UPDM, and DCS.

Fig. 7. Map generated from EO-1 Hyperion data and comparative evaluation of the high-resolution spectra.

low data rates such as IEEE 802.15.4 based protocols which are very commonly used in WSNs with small operating systems such as Contiki [3] and TinyOS[4] that support data collection via multiple hops at a fusion center. An alternative for larger areas is LoRa which is an emerging technology that is particularly well-suited for agricultural applications due to its long range. The $J{\cdot}M$ sensor readings of one snapshot are collected and processed at the fusion center.

While the ranges may suffice for a single agricultural field, on huge areas, especially for calibrating satellite data, cellular networks might be an option in areas with sufficient coverage; many carriers already offer specialized plans for machine-to-machine communication which are affordable when sending small amounts of data from many devices.

6. Conclusion & future work

The evaluations in this paper showed that using multiple multi-spectral sensors with different filters opens up a new way to get hyperspectral data from a WSN. For the calculation of the high-resolution spectrum, DCS showed the best results although it requires less a priori information than UPDM. UPDM is highly dependent on the choice of base spectra, making universal usage difficult, it is only suitable for small networks in areas with homogeneous composition.

In our future work, we want to try the approach in an actual deployment as soon as adequate hardware becomes available. Therein we will mainly tackle calibration challenges. Furthermore, we seek ways to further improve the spectrum reconstruction.

Acknowledgements

We would like to thank Bastian Siegmann and Martin Kanning for supplying us with the in situ and airborne data used in this work and for the sustainable discussions and work.

We would like to thank Alexander Tessmer for the sustainable discussions and work.

The airborne data was acquired by Deutsches GeoForschungsZentrum GFZ.

The satellite data is data available from the U.S. Geological Survey.

[3] http://www.contiki-os.org/.

[4] http://www.tinyos.net/.

References

Baron, D., Duarte, M.F., Wakin, M.B., Sarvotham, S., Baraniuk, R.G., 2009. Distributed Compressive Sensing. CoRR abs/0901.3403. URL https://arxiv.org/abs/0901.3403.

Bauer, J., Aschenbruck, N., 2018. Design and implementation of an agricultural monitoring system for smart farming. In: Proc. of the IoT Vertical and Topical Summit on Agriculture - Tuscany (IOT Tuscany), pp. 1–6. https://doi.org/10.1109/IOT-TUSCANY.2018.8373022.

Candes, E., Wakin, M., 2008. An introduction to compressive sampling. IEEE Signal Process. Mag. 25 (2), 21–30. https://doi.org/10.1109/MSP.2007.914731.

Dale, L.M., Thewis, A., Boudry, C., Rotar, I., Dardenne, P., Baeten, V., Pierna, J.A.F., 2013. Hyperspectral imaging applications in agriculture and agro-food product quality and safety control: A review. Appl. Spectrosc. Rev. 48 (2), 142–159. https://doi.org/10.1080/05704928.2012.705800.

Dell'Acqua, F., Gamba, P., Ferrari, A., Palmason, J.A., Benediktsson, J.A., Arnason, K., 2004. Exploiting spectral and spatial information in hyperspectral urban data with high resolution. IEEE Geosci. Remote Sens. Lett. 1 (4), 322–326. https://doi.org/10.1109/LGRS.2004.837009.

Dobler, G., Ghandehari, M., Koonin, S.E., Sharma, M.S., 2016. A hyperspectral survey of New York City lighting technology. Sensors 16 (12). https://doi.org/10.3390/s16122047.

Donoho, D.L., 2006. Compressed sensing. IEEE Trans. Informat. Theory 52 (4), 1289–1306. https://doi.org/10.1109/TIT.2006.871582.

Duarte, M., Baraniuk, R., 2012. Kronecker compressive sensing. IEEE Trans. Image Process. 21 (2), 494–504. https://doi.org/10.1109/TIP.2011.2165289.

Ehlers, M., Klonus, S., Åstrand, P.J., Rosso, P., 2010. Multi-sensor image fusion for pansharpening in remote sensing. Int. J. Image Data Fusion 1 (1), 25–45. https://doi.org/10.1080/19479830903561985.

Gobbett, D.L., Handcock, R.N., Zerger, A., Crossman, C., Valencia, P., Wark, T., Davies, M., 2013. Prototyping an Operational System with Multiple Sensors for Pasture Monitoring. J. Sensor Actuat. Networks 2 (3), 388–408. https://doi.org/10.3390/jsan2030388.

Hartung, R., Kulau, U., Gernert, B., Rottmann, S., Wolf, L., 2017. On the experiences with testbeds and applications in precision farming. In: Proc. of the First ACM International Workshop on the Engineering of Reliable, Robust, and Secure Embedded Wireless Sensing Systems. FAILSAFE'17, pp. 54–61. https://doi.org/10.1145/3143337.3143338.

Hänel, T., Aschenbruck, N., 2017. Accelerating yield mapping at low data rates using compressive field estimate. In: Proc. of the 42nd IEEE Conference on Local Computer Networks (LCN), pp. 374–382. https://doi.org/10.1109/LCN.2017.56.

Ji, S., Xue, Y., Carin, L., 2008. Bayesian compressive sensing. IEEE Trans. Signal Process. 56 (6), 2346–2356. https://doi.org/10.1109/TSP.2007.914345.

Liu, B., Zhang, L., Zhang, X., Zhang, B., Tong, Q., 2009. Simulation of EO-1 hyperion data from ALI multispectral data based on the spectral reconstruction approach. Sensors 9 (4), 3090–3108. https://doi.org/10.3390/s90403090.

Mohimani, H., Babaie-Zadeh, M., Jutten, C., 2009. A fast approach for overcomplete sparse decomposition based on smoothed ℓ^0 norm. IEEE Trans. Signal Process. 57 (1), 289–301. https://doi.org/10.1109/TSP.2008.2007606.

Mulla, D.J., 2013. Twenty five years of remote sensing in precision agriculture: Key advances and remaining knowledge gaps. Biosyst. Eng. 114 (4), 358–371. https://doi.org/10.1016/j.biosystemseng.2012.08.009. special Issue: Sensing Technologies for Sustainable Agriculture.

Qu, Y., Zhu, Y., Han, W., Wang, J., Ma, M., 2014. Crop leaf area index observations with a wireless sensor network and its potential for validating remote sensing products. IEEE J. Sel. Top. Appl. Earth Obser. Remote Sens. 7 (2), 431–444. https://doi.org/10.

1109/JSTARS.2013.2289931.
Quer, G., Masiero, R., Munaretto, D., Rossi, M., Widmer, J., Zorzi, M., 2009. On the interplay between routing and signal representation for Compressive Sensing in wireless sensor networks. In: Proc. of the Information Theory and Applications Workshop, pp. 206–215. https://doi.org/10.1109/ITA.2009.5044947.
Rudelson, M., Vershynin, R., 2006. Sparse reconstruction by convex relaxation: Fourier and gaussian measurements. In: Proc. of th 40th Ann. Conf. on Information Sciences and Systems (CISS), pp. 207–212. https://doi.org/10.1109/CISS.2006.286463.
Sun, X., Zhang, L., Yang, H., Wu, T., Cen, Y., Guo, Y., 2015. Enhancement of spectral resolution for remotely sensed multispectral image. IEEE J. Sel. Top. Appl. Earth Obser. Remote Sens. 8 (5), 2198–2211. https://doi.org/10.1109/JSTARS.2014.2356512.
van der Meer, F.D., van der Werff, H.M., van Ruitenbeek, F.J., Hecker, C.A., Bakker, W.H., Noomen, M.F., van der Meijde, M., Carranza, E.J.M., de Smeth, J.B., Woldai, T., 2012. Multi- and hyperspectral geologic remote sensing: A review. Int. J. Appl. Earth Obser. Geoinformat. 14 (1), 112–128. https://doi.org/10.1016/j.jag.2011.08.002.
Vivone, G., Alparone, L., Chanussot, J., Mura, M.D., Garzelli, A., Licciardi, G.A., Restaino, R., Wald, L., 2015. A critical comparison among pansharpening algorithms. IEEE Trans. Geosci. Remote Sens. 53 (5), 2565–2586. https://doi.org/10.1109/TGRS.2014.2361734.